The Astrophysical Journal, 988:36 (14pp), 2025 July 20 https://doi.org/10.3847/1538-4357/add691

Rethinking Habitability Using Biogenic Precursors: Formaldehyde in Millimeter Molecular Clouds of the Inner Galaxy

N. B. Baharin[1], A. A. Nazri[1], Z. Rosli[1,2], Z. Z. Abidin[1], H. A. Tajuddin[3], J. Esimbek[4], D. L. Li[4], and X. Tang[4]
[1] Department of Physics, Faculty of Science, Universiti Malaya, 50603 Kuala Lumpur, Malaysia
[2] Centre of Foundation, Language and Malaysian Studies, Universiti Malaya-Wales, 50480 Kuala Lumpur, Malaysia
[3] Department of Chemistry, Faculty of Science, Universiti Malaya, 50603 Kuala Lumpur, Malaysia
[4] Xinjiang Astronomical Observatory, Chinese Academy of Sciences, Urumqi 830011, People's Republic of China
Received 2025 March 26; revised 2025 May 1; accepted 2025 May 2; published 2025 July 11

Abstract

We present a comprehensive study of formaldehyde (H_2CO) absorption and radio recombination line ($H_{110\alpha}$) emission in 215 molecular clouds from the Bolocam Galactic Plane Survey, observed using the Nanshan 25 m radio telescope. H_2CO was detected in 88 sources (40.93%) with 59 being new detections, while $H_{110\alpha}$ emission was found in only 11 sources (5.12%), all coincident with H_2CO absorption. There exists a correlation of H_2CO fluxes with millimeter fluxes below a 3 Jy threshold and an increased dispersion above it, suggesting the sub-cosmic microwave background cooling of H_2CO. Cross-matching with kinematic distance catalogs revealed H_2CO spanning galactocentric distances from 0.216 to 10.769 kpc, with column densities ranging from 7.82×10^{11} to 6.69×10^{14} cm^{-2}. A significant inverse correlation was observed between H_2CO detection fraction and galactocentric distance, suggesting enhanced star-forming activity closer to the Galactic Center. These findings challenge traditional Galactic Habitable Zone (GHZ) models by demonstrating the presence of biogenic precursors in the inner Galaxy, shielded within dense molecular clouds. Our results underscore the importance of incorporating chemical tracers such as H_2CO, alongside physical constraints to refine the boundaries of the GHZ and advance the research of prebiotic chemistry in the Milky Way.

Unified Astronomy Thesaurus concepts: Star forming regions (1565); Radio spectroscopy (1359); Pre-biotic astrochemistry (2079); Habitable zone (696)

Materials only available in the online version of record: machine-readable tables

1. Introduction

W. H. Tucker (1981) initially presented how supernovae and gamma-ray bursts could sterilize regions of the galaxy by exposing planets to intense radiation, and so laid the groundwork for the concept of an annular Goldilocks area in the disk of a galaxy that is "just right" for life to form. G. Gonzalez et al. (2001) and G. Gonzalez (2005) then further refined the concept of a Galactic Habitable Zone (GHZ) by incorporating factors such as metallicity, stellar density, and the frequency of catastrophic events. Now, GHZ is being increasingly utilized for the discovery of exoplanets (N. Nari et al. 2025), explorations of habitability of M-dwarfs in the galaxy (S. Sagear & S. Ballard 2023), and likelihood of terrestrial planets to form around a parent star (M. Gowanlock et al. 2011), thus making essential the efforts in constraining the inner and outer radii of the GHZ. The accepted borders of the GHZ of Milky Way are within approximately 7–10 kpc from the Galactic Center, with 75% of the stars older than the Sun, aged 8–4 Gyr (C. H. Lineweaver et al. 2004), with its inner boundary being constrained by radiation hazards, and the outer line being limited by insufficient metallicity for planet formation (G. Gonzalez et al. 2001). E. Spitoni et al. (2014) widened the GHZ acreage to 8–12 kpc from the Galactic center, peaking at 10 kpc when taking into account the higher number of stars with habitable environments that formed in the inner regions due to weaker radial gas inflows but it is followed by the postulation that the GHZ started as a narrow band at large radii, and then settles into a range of 2–13 kpc, as exhibited by a three-dimensional, asymmetric modeling of the temporal evolution of GHZ (D. Forgan et al. 2016). In limiting the outer boundary of the GHZ, *N*-body simulation models of the GHZ by B. Vukotić et al. (2016) predicted stellar particles with mass of $5 \times 10^4 M_\odot$ inhabit regions of ~16 kpc for most of their lifetimes and so implies areas in the 10–15 kpc range to be most feasible in harboring habitable systems. Conversely, Monte Carlo modeling methods by M. Gowanlock et al. (2011) interestingly pull back the inner radius of GHZ to a minimum of $R < 4.1$ kpc and above the disk's midplane at $z \approx 1.5$ kpc, since this is the region with the greatest fraction of stars with habitable planets when considering sufficient planet-forming levels of metallicity and stellar density that negate the impact of supernova sterilizations.

However, it has also been proposed that the inner radius of GHZ could even encompass the Galactic bulge (A. Balbi et al. 2020) as it considers the broad metallicity distribution in the inner 2 kpc of the bulge, ranging from $Z = -0.1$ to 0.4 and the time between projected supernova (SN)-induced mass extinction events, around 40 and 110 Gyr^{-1}. N. Prantzos (2007) modeled stellar distribution containing solar-like systems in five epochs throughout the Galaxy's evolution and found that all metallicity-dependent probabilities peak early in the inner disk and due to the inside-out formation pattern of the Milky Way, spread toward the outer limits of the galaxy and in the time it took to do so the absolute probability value of surviving SN explosions would be substantial in the inner disk, and so

cursorily opined the entire Milky Way disk could be a habitable zone.

Another method of constraining the boundaries of a GHZ is by chemically mapping Milky Way regions for biogenic molecules to identify areas in which the necessary reactions ostensibly occur in order to produce complex organic molecules (COMs) that can then sequentially give rise to amino acids and proteins, the building blocks for life. Contrary to their name, COMs are only defined as complex in the context of the environment in which these species interact, such as the interstellar medium and star-forming regions (SFRs), but are fundamentally compounds containing at least six atoms with a backbone of carbon, and are usually found in dense, cold molecular clouds (MCs) that act as reservoirs and natural shields, allowing their formation and preservation (E. Herbst & R. T. Garrod 2022). As noted by L. M. Ziurys (2018), interstellar molecules e.g., formaldehyde (H_2CO) and methanol (CH_3OH), are critical precursors to life and their distribution throughout the galaxy by way of a molecular lifecycle mechanism should be a key factor in defining the GHZ. Prebiotically plausible molecules have been detected as far as 23.6 kpc (Edge Cloud 2), low metallicity and enhanced cosmic ray ionization rates notwithstanding (P. M. E. Ruffle et al. 2007). At distances >16 kpc, the far outer Galaxy is characterized by lower gas and stellar densities, weaker interstellar radiation fields, and fewer supernova remnants to trigger star formation, and yet a significant number of MCs are observed in place of nebulous medium (e.g., R. L. Snell et al. 2002; C. M. Brunt et al. 2003). It is with this reasoning that S. K. Blair et al. (2008) surveyed galactic MCs for H_2CO in an attempt to reconfigure the outer limits of the habitable region and found H_2CO observable in MCs at $R_{gal} > 20$ kpc. CH_3OH has also been cited as a potential precursor to larger organic species, such as glycoaldehyde (A. Coutens et al. 2015), acetic acid (M. D. Boamah et al. 2014), and ethylene glycol (C. Zhu et al. 2020), while also being deemed a species most likely to survive in benign environments, leading to it being proposed as a viable criterion for defining the GHZ, for which J. J. Bernal et al. (2021) found its range of detection to be a compelling $R_{gal} = 12.9$–23.5 kpc.

Since its discovery (L. E. Snyder et al. 1969), interstellar H_2CO has been extensively studied as a biogenic precursor, given its association with numerous biochemically relevant processes (P. Ehrenfreund et al. 2002; P. Caselli & C. Ceccarelli 2012, e.g.,). Its presence is closely linked to the GHZ, suggesting the potential for life-bearing environments in regions enriched with H_2CO (S. K. Blair et al. 2008). Protoplanetary disks inherit and preserve H_2CO-containing interstellar ice, providing evidence for the presence of prebiotic precursor molecules in planet-forming regions (L. Evans et al. 2025). A. F. Punanova et al. (2025) most recently confirmed that the formation of H_2CO is directly connected to the formation of methanol (CH_3OH), which is often referred to as the simplest COM and acts as an abundance reference for other COMs. G. Costanzo et al. (2007) detailed H_2CO's role in a specific chemomimetic reaction to synthesize components of nucleic acid in the form of formamide (NH_2CHO) as an in situ precursor, which motivated G. R. Adande et al. (2013) to target MC regions harboring compact hot cores and found widespread NH_2CHO distribution in locations ranging from 0.13 to 9.6 kpc, with its greatest possibility of life at a radius of about 2.5 kpc. As such, this necessitates research geared toward constraining the GHZ according to the limits of where H_2CO is found. The currently accepted inner and outer limits of the GHZ are about 7–9 kpc from the Galactic Center (N. Prantzos 2007; M. Gowanlock et al. 2011) with our Sun in a serendipitous location of 8 kpc.

While H_2CO has been scantily detected in the outer Galaxy (S. K. Blair et al. 2008) and toward the Galactic center (A. Sandqvist & C. Bernes 1980), systematic studies of its distribution in the inner Galaxy are limited. The chemical environment in the neighborhood of the region remains underexplored as sporadic studies discuss separate molecules within limited ranges and are currently insufficient to wholly define the GHZ in terms of its chemical composition. Current habitability models also heavily focus on metallicity and probability to survive annihilating events, but often overlook the role of biogenic precursors in defining these zones. Building on existing studies, by now focusing on the presence of H_2CO in the inner Galaxy i.e., <7 kpc, one of the richest repositories of COMs in the Galaxy (e.g., S. Zeng et al. 2018), we intend to ascertain to what extent the established inhibitors of habitability affect the synthesis and survival of formaldehyde deeper in the Galaxy, if there are regions in the inner galaxy where prebiotic molecules are shielded from destructive processes, if the presence of significantly abundant formaldehyde in the inner galaxy could speculatively redefine the boundaries of the GHZ, and mainly to contribute to the usage of prebiotically plausible molecules in honing the contemporary definition of a GHZ as a whole.

This paper is structured as follows. In Section 2, we describe the sample selection, observational methods, and data analysis. We present the results of our observation as well as preliminary discussions in Sections 3 and 4, respectively. Section 5 then underlines our procedures in determining the physical parameters of our sample, primarily the galactocentric distances and column densities, while Section 6 discusses the correlations presenting from said parameters. Finally, in Section 7 we extensively deliberate on the implications of our results on the current understanding of the GHZ bounds.

2. Methodology

2.1. Sample Selection

The MC sample was drawn from the Bolocam Galactic Plane Survey (BGPS; J. E. Aguirre et al. 2010), which mapped a 170 deg^2 region of the Galactic plane in the 1.1 mm continuum using the Caltech Submillimeter Observatory. The survey cataloged 8358 compact sources, with a 98% completeness level for flux densities between 0.4 and 60.0 Jy (E. Rosolowsky et al. 2010). To refine our sample, we selected sources with flux densities in the range $1\ \mathrm{Jy} < S_{\mathrm{BGPS}} < 10\ \mathrm{Jy}$ and restricted the Galactic latitude to $\|b\| < 1°$. Furthermore, we ensured that each selected source was spatially isolated by requiring the angular separation from its nearest neighbor to exceed the telescope's beam size (described in the following subsection). This selection yielded a final sample of 215 sources.

2.2. Observations

The observations of the selected MCs were conducted using the Nanshan 25 m radio telescope,[5] operated by the Xinjiang

[5] The telescope has since been upgraded to 26 m, as of late-2015.

Astronomical Observatory in Urumqi, China (43°28′17″N, 87°10′41″E), situated at an altitude of 2080 m above sea level. The telescope is equipped with a *C*-band cryogenic receiver with a system temperature of 23 K. It offers a beam efficiency of 65% and achieves a pointing and source tracking accuracy of better than 15″. The full width at half-maximum (FWHM) of the primary beam at the telescope operating frequencies is approximately 10′. A diode noise source was employed to calibrate the spectrum at the start of each observation period, with flux calibration uncertainties within 10%.

The observations were carried out between 2012 November and 2014 February using the Digital Filter Bank for spectrometry. The frequency setup was centered at 4851.9102 MHz, with a bandwidth of 64 MHz divided into 8192 channels, corresponding to a spectral and velocity resolution of 7.8 kHz and 0.48 km s^{-1}, respectively. Rest frequencies of 4829.6594 MHz and 4874.1570 MHz were adopted to measure the velocities of H_2CO ($K_a = 1_{10}$–1_{11}) absorption and $H_{110\alpha}$ emission. Observations were conducted in the ON/OFF mode. Each source was initially observed with a 24 minutes integration, with an additional 24 minutes integration performed if the signal-to-noise ratio was found to be less than 3. To ensure the system's reliability, the W3 giant MC was observed as a reference source.

2.3. Data Reduction

The spectral data were reduced using the CLASS software, which is part of the Grenoble Image and Line Data Analysis Software package. Baseline subtraction using polynomial baselines was applied to all spectra before fitting Gaussian profiles to the detected lines, with negative profiles for H_2CO absorption and positive profiles for $H_{110\alpha}$ emission. Gaussian fits were performed for spectral features above 3σ (peaks above 2.5σ were also considered on a case-by-case basis).

2.4. BGPS-H_2CO Cataloging

To further analyze the selected BGPS sources and their results, we associate each with a single H_2CO line and a single $H_{110\alpha}$ line, if detected. In cases where multiple features are present, we select the one with the highest brightness temperature. Line fluxes are then derived using the Rayleigh–Jeans approximation, assuming the telescope's beam FWHM represents the angular extent of each source.[6] We refer to this catalog as the BGPS-H_2CO catalog, shown in Table 6.

3. Results

A list of all the selected 215 BGPS sources with their H_2CO and $H_{110\alpha}$ detection flags are shown in Table 2. In total, 88 of the sources were detected with H_2CO absorption (40.93%), and 11 of those sources also possess $H_{110\alpha}$ emission (5.12%). None of the sources were detected with only $H_{110\alpha}$ lines. Observational parameters for sources with detections are listed in Table 3. A total of 183 H_2CO absorption lines were detected, with 56 sources (64.64%) exhibiting more than one spectral feature. An example spectrum of a source displaying H_2CO absorption is presented in Figure 1. Each detected H_2CO line is assigned an MC number. The corresponding Gaussian fitting results for all MCs are summarized in Table 4. A total of 13 $H_{110\alpha}$ emission lines were identified, with two sources (BGPS2094 and BGPS5910) displaying double-peaked profiles (18.18%). Figure 2 illustrates a representative spectrum of a source exhibiting both $H_{110\alpha}$ emission and H_2CO absorption. Each detected $H_{110\alpha}$ line is assigned an HII region identifier, with their Gaussian fitting results provided in Table 5. The statistics of the Gaussian-fitted parameters for both H_2CO and $H_{110\alpha}$ lines are presented in Table 1, while Figure 3 visualizes the distributions of brightness temperatures, velocities, and line widths for all fitted profiles.

To comprehensively compare our results with known detections, we compiled all available literature reporting positive detections of the H_2CO ($K_a = 1_{10}$–1_{11}) absorption line in the Milky Way to produce an extended H_2CO list. W. H. Guo et al. (2016, G16 hereafter) previously cataloged all 4.8 GHz H_2CO absorption detections up to 2014 March, totaling 2241 unique sources. Since then, a few additional detections have been reported toward various astrophysical environments, including low- and high-mass star-forming regions (E. D. Araya et al. 2015; X. Chen et al. 2017; Y. Gong et al. 2023), MCs (Y. T. Yan et al. 2019), and giant MCs (A. Ginsburg et al. 2015a; T. Komesh et al. 2019; U. Mahmut et al. 2024).

Shown in Figures 4 and 5 are comparisons of the distributions of H_2CO absorption fluxes for BGPS-H_2CO with G16 and with the other catalogs, respectively. The fluxes in BGPS-H_2CO falls within the range of G16, with a mean value within an order of magnitude i.e., 0.463 Jy and 0.869 Jy respectively. Similarly, the flux distribution of BGPS-H_2CO also aligns well with that of the other catalogs, exhibiting a comparable range. In particular, the results from observations using the Nanshan telescope (T. Komesh et al. 2019; U. Mahmut et al. 2024) closely match those of BGPS-H_2CO. Observations using telescopes with larger diameters (e.g., Arecibo Telescope, E. D. Araya et al. 2015; A. Ginsburg et al. 2015a; Tianma Radio Telescope, Y. T. Yan et al. 2019) were able to detect H_2CO at lower fluxes due to their higher sensitivity. Figure 6 shows the distribution of H_2CO absorption fluxes and line FWHM for BGPS-H_2CO compared to G16, and the line parameters in BGPS-H_2CO are consistent. After cross-matching the extended H_2CO list with our BGPS-H_2CO catalog, we found that 59 out of the 88 BGPS-H_2CO sources are newly detected.

4. Discussion

4.1. Coincident H_2CO and $H_{110\alpha}$ Detections

Based on our results, there were no detections of $H_{110\alpha}$ without an accompaniment of H_2CO, and only 11 (12.5%) of the sources possessing H_2CO absorption also have $H_{110\alpha}$ emission line(s). Radio recombination lines (RRLs) and H_2CO are not typically detected in the same regions because they usually originate from fundamentally different environments. RRLs trace hot (∼10,000 K), ionized gas in H II regions, which are created and maintained by ultraviolet (UV) radiation from massive stars. In contrast, H_2CO absorption lines come from cold, dense molecular gas shielded from UV radiation. The intense UV radiation in H II regions destroys molecules such as H_2CO, establishing a sharp boundary between ionized and molecular gas (D. J. Hollenbach & A. G. G. M. Tielens 1999).

As for the BGPS sources with both detections, multiple explanations are possible. Photodissociation regions in massive SFRs allows for the coexistence of ionized and molecular

[6] Although these fluxes are negative, our analyses consider them as positive values for simplicity, which we refer to as H_2CO absorption fluxes.

Table 1
Statistics of Gaussian-fitted Parameters for H_2CO and $H_{110\alpha}$ Lines Detected

Line	H_2CO			$H_{110\alpha}$		
Parameter	Flux (K)	Velocity (km s^{-1})	FWHM (km s^{-1})	Flux (K)	Velocity (km s^{-1})	FWHM (km s^{-1})
Minimum	−0.012	−73.71	0.88	0.013	−46.76	10.69
	BGPS2864 MC1	BGPS2864 MC1	BGPS5813 MC2	BGPS5910 H II a	BGPS6661 H II a	BGPS5910 H II b
Maximum	−0.335	216.30	50.45	0.091	109.90	31.98
	BGPS0512 MC4	BGPS0548 MC4	BGPS0927 MC1	BGPS2094 H II b	BGPS4372 H II a	BGPS4372 H II a
Mean	−0.069	40.56	7.00	0.032	54.30	23.07
Median	−0.050	38.77	4.12	0.024	59.28	23.31

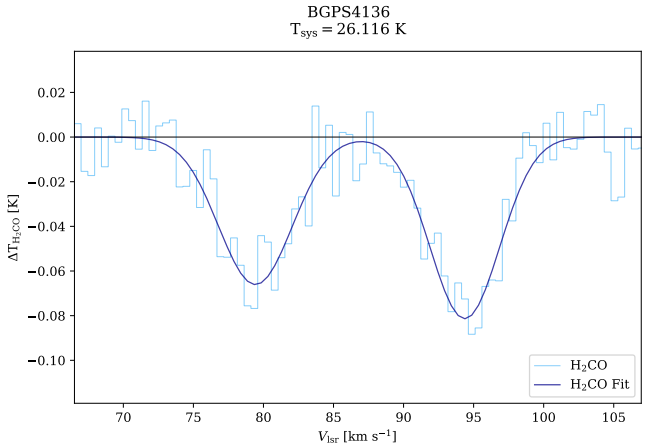

Figure 1. Spectrum of BGPS4136 showing H_2CO absorption lines. The gray area denotes the 1σ baseline noise. Note that this source does not possess any $H_{110\alpha}$ lines and therefore is not included in the plot.

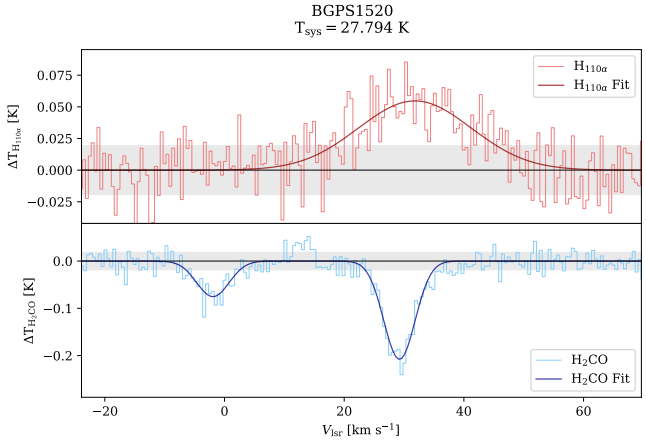

Figure 2. Spectrum of BGPS1520 showing a $H_{110\alpha}$ emission line (in the top panel, and H_2CO absorption lines in the bottom panel). Similar to Figure 1, the gray area denotes the 1σ baseline noise.

gases, usually in the boundaries of H II regions (D. J. Hollenbach & A. G. G. M. Tielens 1999). However, pressure-driven expansion of the H II region can further separate them, leading to a rarefied ionized region and molecular gas dominance in surrounding clouds (E. Keto 2002). The presence of dense gases in molecular clumps can also shield H_2CO from the strong UV radiation, preventing its destruction (S. Cuadrado et al. 2017). In young and complex massive star-forming regions, localized areas with varying physical conditions can exist in close proximity, particularly when ionized gas has not yet fully dispersed the surrounding MC (e.g., J. Bally & N. Z. Scoville 1980). Additionally, since massive stars are intrinsically rare according to the stellar mass function, such unique regions are relatively uncommon.

As for the line parameters, no correlation was seen between the H_2CO absorption fluxes and $H_{110\alpha}$ emission fluxes. Similarly, the FWHMs of the coincident lines do not exhibit any direct relationship, but $H_{110\alpha}$ lines generally exhibit broader FWHMs than H_2CO. The median FWHM of $H_{110\alpha}$ emission is 23.31 km s^{-1}, consistent with previous observations of $H_{110\alpha}$ in H II regions (e.g., C. Quireza et al. 2006). In comparison, the median FWHM of H_2CO absorption is 4.12 km s^{-1}, exceeding the range expected from thermal broadening and hyperfine structure effects (see Y. Yuan et al. 2014; W. H. Guo et al. 2016). The broader widths of RRLs are primarily attributed to turbulence and large-scale ordered motions within MCs. In young H II regions, the presence of large-scale ionized gas motions around the central protostar also contributes to the line broadening (M. Sewilo et al. 2004; E. Keto et al. 2008). In contrast, molecular lines, including H_2CO, generally have narrower FWHMs because molecular gas is less spatially extended than H I and H II regions (K. M. Menten & M. J. Reid 1996; E. W. Koch et al. 2019).

Shown in Figure 7 is the relation between the H_2CO and $H_{110\alpha}$ line velocities in sources with coincident detections. The H_2CO velocities correlate close to a 1:1 relation with the $H_{110\alpha}$ velocities with a high correlation coefficient, suggesting that H_2CO and $H_{110\alpha}$ trace the same physical properties of each MC (S. Khan et al. 2024; C. H. M. Pabst et al. 2024).

4.2. Millimeter and H_2CO Absorption Flux

Shown in Figure 8 is the comparison of the H_2CO absorption and $H_{110\alpha}$ emission fluxes with the 1.1 mm BGPS fluxes. The relationship between H_2CO flux and 1.1 mm continuum flux in BGPS-H_2CO exhibits significant dispersion, with an overall very weak correlation ($r = 0.1376$). However, when separating the catalog at a 3 Jy threshold, a moderate correlation is present in both the low and high flux regimes ($r = 0.2968$ and $r = 0.3528$, respectively).[7] Each section has different slopes, and this bears resemblance to the results of X.-D. Tang et al. (2014) who found that H_2CO absorption correlates with 6 cm continuum at low flux levels but eventually becomes more scattered at high fluxes, likely due to changing excitation conditions. However, while their study focused on radio continuum, our work examines the relationship between H_2CO flux and 1.1 mm far-infrared continuum,

[7] The flux threshold is obtained by testing over all possible flux levels and maximizing both correlation coefficients.

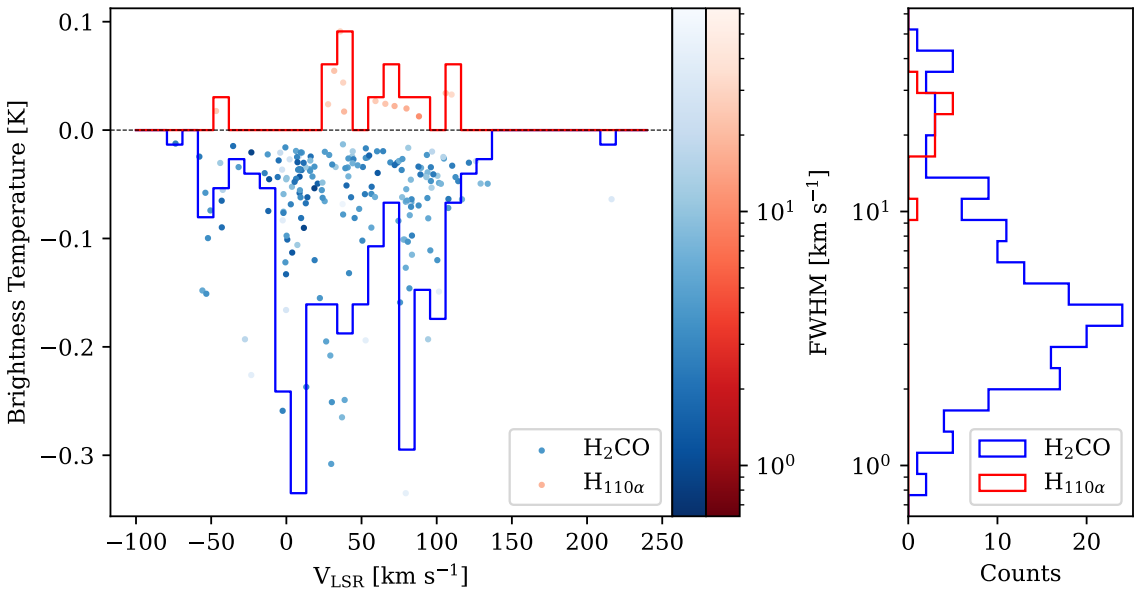

Figure 3. Distribution of parameters for all Gaussian-fitted H_2CO and $H_{110\alpha}$ lines. Left: Plot of the lines' brightness temperatures against their central velocities, with colors corresponding to their FWHM. The histograms represent the distribution of the lines' velocities; blue for H_2CO and red for $H_{110\alpha}$. Right: Distribution of the FWHM of the lines.

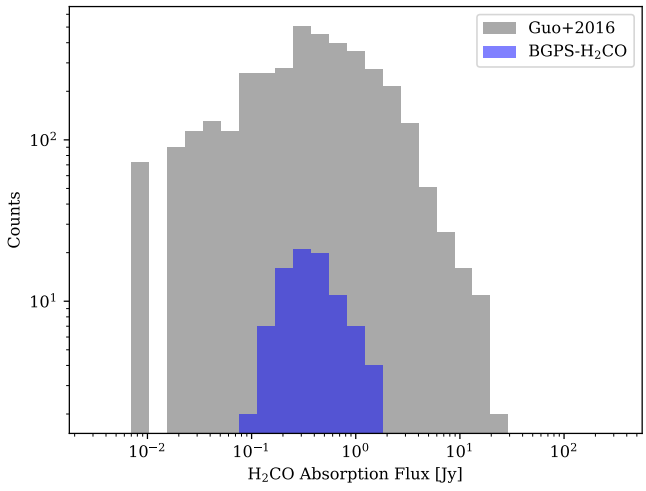

Figure 4. Distribution of H_2CO absorption fluxes for G16, labeled Guo+2016 and our BGPS-H_2CO cataloged.

suggesting that different physical mechanisms may be involved.

Several previous studies have investigated the link between H_2CO absorption and infrared flux at shorter wavelengths, generally finding weak or moderate correlations as well. Z. M. Du et al. (2011) identified two branches in the relation between H_2CO and 100 μm infrared flux—a strong correlation for sources with $H_{110\alpha}$ detections, and a weaker, more dispersed correlation for sources with only H_2CO absorption. Y. Yuan et al. (2014) also found a similar trend but with sources without $H_{110\alpha}$ emission exhibiting no significant dependence. W. H. Guo et al. (2016) noted that higher-resolution observations significantly improved the correlation strength, emphasizing the role of beam dilution in these observations. Our results, which show a moderate correlation when split into two categories, are consistent with these trends. This suggests that while the far-infrared continuum may contribute to H_2CO excitation, additional effects, e.g., local radiation fields and gas density variations, likely play a role in the observed dispersion.

One possible interpretation is that at low far-infrared fluxes, the H_2CO absorption is more dependent on the cosmic microwave background (CMB), resulting in a moderately strong correlation (e.g., H. S. Liszt & J. Pety 2016). C. H. Townes & A. C. Cheung (1969) first proposed a sub-CMB cooling mechanism of H_2CO that allows for effective absorption at low temperatures, and since has been confirmed by various observations (e.g., N. Troscompt et al. 2009; J. Darling & B. Zeiger 2012). However, as the continuum flux increases, additional effects such as optical depth variations, local heating, and changes in H_2CO column density introduces more complexity. Various models have suggested that strong background continuum emission can heat up H_2CO and modify its excitation, potentially leading to partial thermalization of the absorption line (X.-D. Tang et al. 2014; J. Bu et al. 2024; M. Gerin et al. 2024). In more extreme cases, H_2CO maser emission has been detected from multiple high-mass SFRs (e.g., E. D. Araya et al. 2008; A. Ginsburg et al. 2015b). Observations and simulations have also shown that H_2CO excitation temperature can increase above the CMB when electron fractions are high (B. E. Turner 1993; M. Gerin et al. 2024). These stacking dependencies result in the breakdown in the correlation at higher fluxes, and consideration of various nonlocal thermodynamic equilibrium effects may help clarify the anomaly.

5. Derived Parameters

To study our H_2CO results in the context of GHZ, we derive two parameters—the galactic location of our catalog and the physical parameters of the H_2CO detection.

5.1. Kinematic and Galactocentric Distance Cross-Matching

The first step in examining the galactic location dependence of BGPS-H_2CO properties is to determine each source's galactocentric distance, i.e., its distance to the Galactic Center.

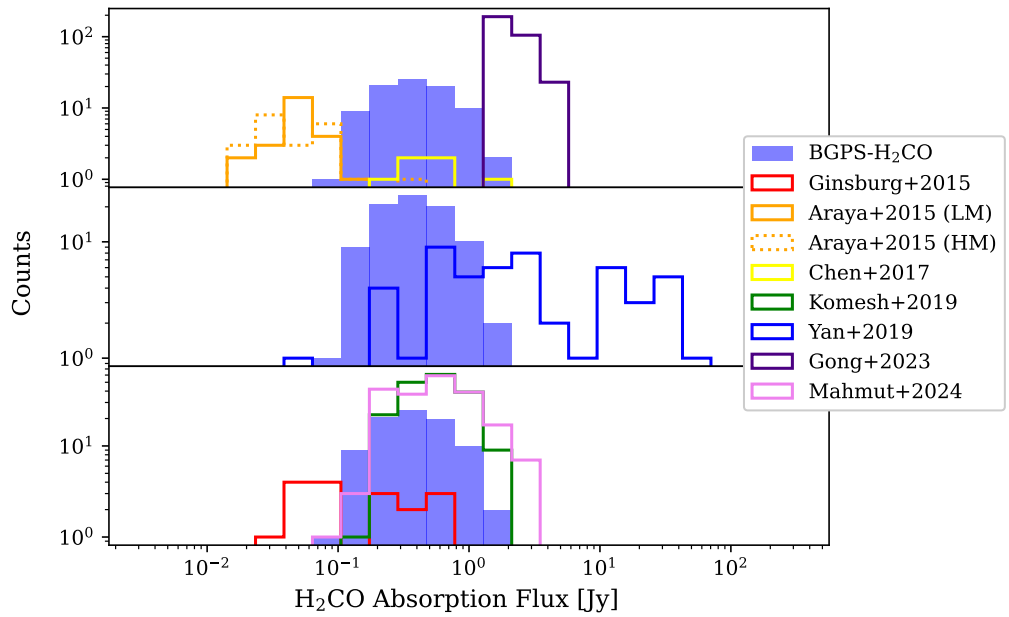

Figure 5. Distribution of H_2CO absorption fluxes for literature after 2014 March and BGPS-H_2CO. References: A. Ginsburg et al. 2015a (Ginsburg+2015), E. D. Araya et al. 2015 (Araya+2015, LM and HM represent low-mass and high-mass SFRs respectively), X. Chen et al. 2017 (Chen+2017), T. Komesh et al. 2019 (Komesh+2019), Y. T. Yan et al. 2019 (Yan+2019), Y. Gong et al. 2023 (Gong+2023), and U. Mahmut et al. 2024 (Mahmut+2024).

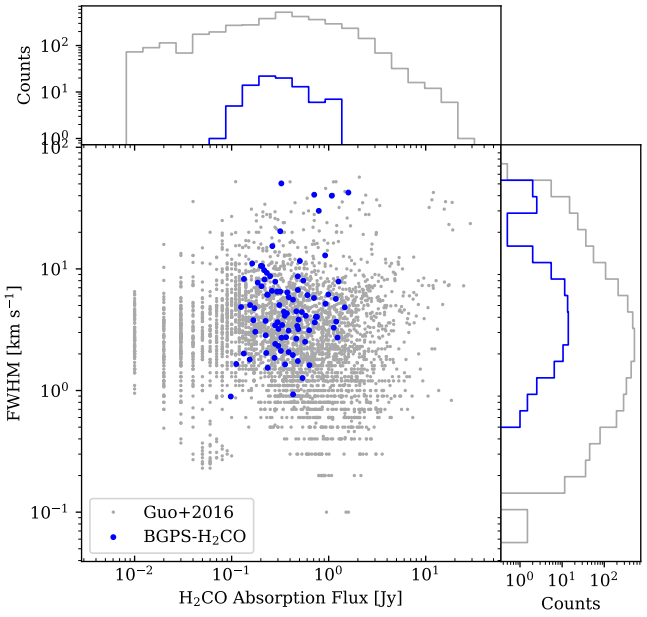

Figure 6. Distribution of H_2CO absorption flux and FWHM for G16, labeled Guo+2016 and BGPS-H_2CO.

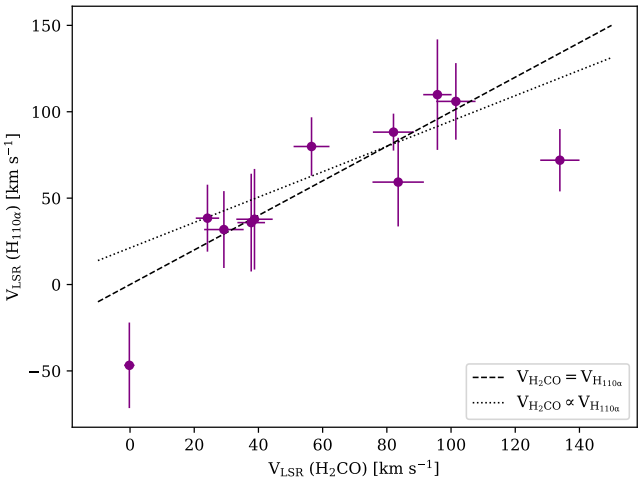

Figure 7. Comparison between H_2CO and $H_{110\alpha}$ line velocities in BGPS-H_2CO. The dashed line represents an exact velocity correlation, while the dotted line represents a best-fit linear relation: $V_{LSR}(H_{110\alpha}) = (0.73 \pm 0.18) \times V_{LSR}(H_2CO) + (21.2 \pm 12.7)$ km s^{-1}. The Pearson's correlation coefficient for this fit is 0.8030.

The most accurate method for this involves parallax measurements of star-forming regions using very long baseline interferometry (see M. Reid & M. Honma 2014), though this approach is resource-intensive. Alternatively, kinematic distances (KDs) can be estimated using the source's V_{LSR} and a Galactic rotation model, either through analytical solutions (L. D. Anderson et al. 2012) or Monte Carlo methods (T. V. Wenger et al. 2018). However, in the inner Galaxy, the kinematic distance ambiguity (KDA) introduces additional challenges due to the two possible solutions for KD. This ambiguity can often be resolved using H I self-absorption (M. A. Kolpak et al. 2003; J. Roman-Duval et al. 2009) or Bayesian inference techniques (M. J. Reid et al. 2019).

However, the limited number of $H_{110\alpha}$ detections in our BGPS-H_2CO sample precludes statistically robust analysis for their KD. Additionally, the usage of H_2CO absorption lines for KD and KDA resolution has proven to be somewhat unreliable, primarily due to the lower filling factor of molecular gas compared to atomic gas (see M. A. Kolpak et al. 2003).

To overcome these challenges, we adopt the MC catalog compiled by M.-A. Miville-Deschênes et al. (2017, MD17 hereafter), which is based on the Milky Way ^{12}CO 1–0 survey conducted by T. M. Dame et al. (2001). The authors identified MCs within $|b| < 5^\circ$ by applying a hierarchical clustering algorithm and Gaussian decomposition to the CO maps. The kinematic distance of each cloud was then derived using the standard V_{LSR} method (J. Roman-Duval et al. 2009), while the

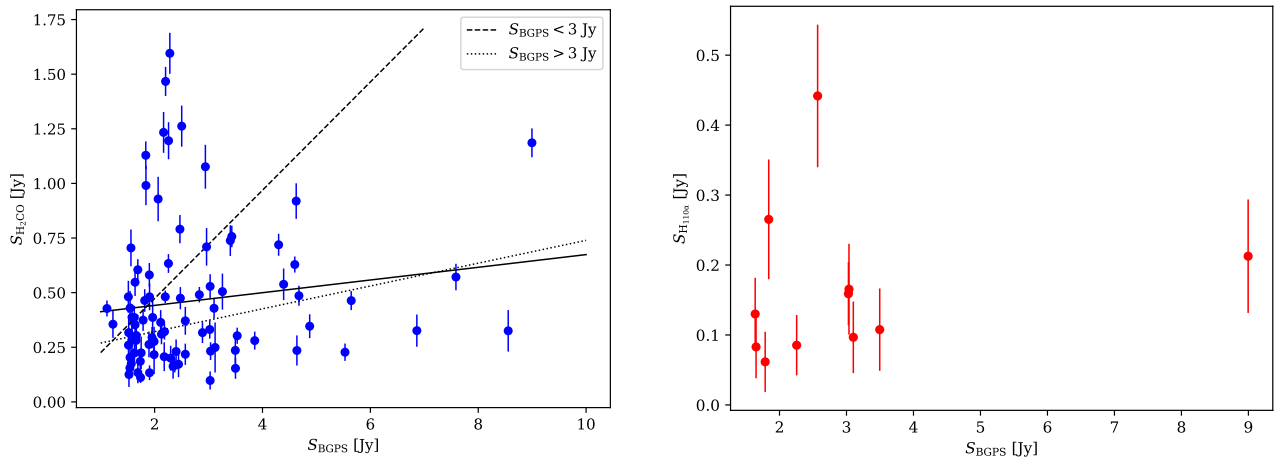

Figure 8. Comparison between BGPS fluxes with H_2CO and $H_{110\alpha}$ fluxes in BGPS-H_2CO. Left: Plot of H_2CO against BGPS 1.1 mm fluxes. The solid line represents the best-fit linear relation: $S_{H_2CO} = (0.03 \pm 0.02) \times S_{BGPS} + (0.38 \pm 0.07)$ Jy. The dashed and dotted lines show separate linear fits for sources below and above the 3 Jy threshold, given by $S_{H_2CO} = (0.25 \pm 0.10) \times S_{BGPS} + (-0.02 \pm 0.21)$ Jy and $S_{H_2CO} = (0.05 \pm 0.03) \times S_{BGPS} + (0.22 \pm 0.14)$ Jy, respectively. The Pearson's correlation coefficients for all three relations are 0.1376, 0.2968, and 0.3528 respectively. Right: Plot of $H_{110\alpha}$ against BGPS 1.1 mm fluxes. The Pearson's correlation coefficient for this relation is 0.1556.

KDA is resolved using a modified version of Larson's scaling relation, incorporating surface density effects i.e., $\sigma_v \propto (R\Sigma)^{0.43}$ (M. Heyer et al. 2009).

To assign KDs and galactocentric distances to our BGPS-H_2CO sources, we cross-matched the BGPS-H_2CO catalog (including nondetections) with the MD17 data set, using a matching threshold based on our instrument's beam FWHM. This resulted in successful cross-matching of 164 out of 215 sources, including 70 with detected H_2CO emission. Notably, all 11 sources exhibiting $H_{110\alpha}$ lines were also successfully matched. The results of the cross-matching are appended within the master BGPS-H_2CO catalog in Table 6.

5.2. H_2CO Column Density Calculations

To further quantify the physical properties of the sources in BGPS-H_2CO, we derive their column densities following a similar methodology to U. Mahmut et al. (2024). The apparent optical depth, τ_{app}, is estimated using standard radiative transfer principles:

$$\tau_{app} = -\ln\left(1 + \frac{T}{T_c + T_{cmb} - T_{ex}}\right), \quad (1)$$

where T, T_c, $T_{cmb} = 2.725$ K, and T_{ex} denote the line brightness temperature, continuum temperature, CMB temperature, and excitation temperature, respectively. For simplicity, we assume the sources lack strong 6 cm continuum emission and adopt an excitation temperature of 1 K, and then apply the approximation $\tau \approx \tau_{app}$ (A. Ginsburg et al. 2015a). Using this optical depth, the H_2CO column density for each BGPS-H_2CO source is then determined following J. G. Mangum & Y. L. Shirley (2015) and U. Mahmut et al. (2024):

$$N_{H_2CO} = 7.3 \times 10^{23}\,\mathrm{cm^{-2}} \times \int \tau\, d\nu, \quad (2)$$

where $\int d\nu$ represents the FWHM of the detected H_2CO line. The derived parameters are appended within the master BGPS-H_2CO catalog in Table 6.

6. H_2CO Relation with Galactic Location

In total, 164 out of all of the 215 sources in the master BGPS-H_2CO catalog were successfully cross-matched with an MD17 counterpart, with 70 of them exhibiting H_2CO absorption, including all 11 sources that also show $H_{110\alpha}$ emission. The closest source to the Galactic center, BGPS0523 is located at a galactocentric radius of 0.216 kpc and exhibits H_2CO absorption but no $H_{110\alpha}$ emission. In contrast, the most distant H_2CO detection, BGPS7120 is found to be at 10.769 kpc, while BGPS5703 is the farthest cross-matched source from the Galactic center at 16.270 kpc, but with no detected H_2CO or $H_{110\alpha}$ emission. For completeness, we also report that the closest source to the Galactic center with nondetections of both lines is BGPS0352 at 0.219 kpc. Figure 9 describes the H_2CO and $H_{110\alpha}$ detection fraction with respect to their galactocentric distance.

Figure 10 shows the distribution of H_2CO column densities for our BGPS-H_2CO sample. The H_2CO column densities obtained for BGPS-H_2CO sources are within the range of 7.82×10^{11} to $6.69 \times 10^{14}\,\mathrm{cm^{-2}}$, with a median value of $1.51 \times 10^{13}\,\mathrm{cm^{-2}}$. These values are consistent with those reported in MC surveys (e.g., Y. T. Yan et al. 2019) and targeted MC observations (Y. Gong et al. 2023; U. Mahmut et al. 2024), even across different transitions (e.g., X. Zhao et al. 2024). For massive star-forming regions in particular, the column densities agree with those of high-mass starless cores, but are approximately 2–3 dex lower than more evolved stages such as high-mass protostellar objects and ultracompact H II regions (S. Zahorecz et al. 2021). This supports the notion that the BGPS-H_2CO objects are indeed in the early stages of star formation.

Consequently, 70 BGPS-H_2CO sources with associated galactocentric distances also have calculated column densities. Shown in Figure 11 is the relation between BGPS-H_2CO galactocentric distances and their column densities. The H_2CO detection fractions (see Figure 9) and column densities both inversely correlate with galactocentric distance. Since H_2CO commonly traces star formation, this indicates that such activities are more prominent closer to the Galactic center, distancing the notion that star formation is suppressed in such extreme environments.

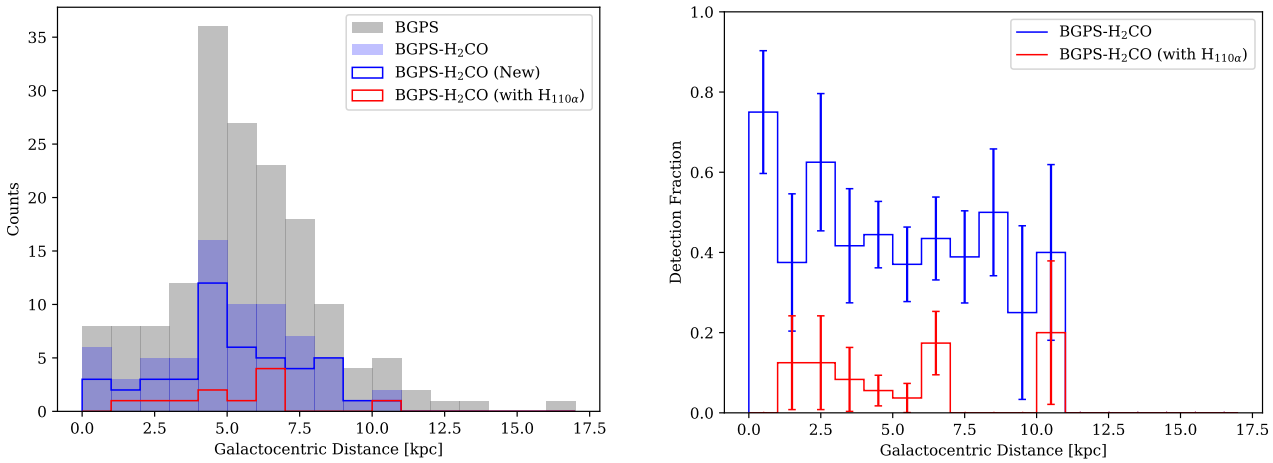

Figure 9. Results of cross-matching between our BGPS sample and the MD17 catalog. Right: Distribution of galactocentric distance for all the cross-matched BGPS sources in our sample. Left: Plot of H_2CO and $H_{110\alpha}$ detection fraction against galactocentric distance for all the cross-matched BGPS sources in our sample. The Pearson's correlation coefficients for the H_2CO and $H_{110\alpha}$ detection fraction against galactocentric distance are −0.8822 and −0.4192, respectively.

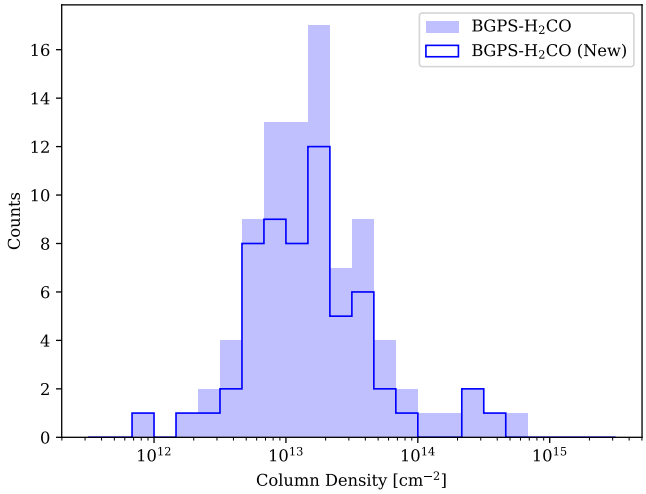

Figure 10. Distribution of calculated column densities from our BGPS-H_2CO catalog.

One possible interpretation for the correlations is the presence of common fueling mechanisms for both active galactic nuclei (AGNs) and star formation. Tidal torques induced by mergers of gas-rich galaxies, i.e., *wet mergers*, can drive rapid inflows of gas within galaxies (P. F. Hopkins et al. 2008). Similarly, close interactions between galaxies of comparable masses can channel molecular gases toward the center of these galaxies (E. Koulouridis et al. 2006). Secular processes such as the formation and/or instability of galactic bars and bulges can also facilitate gas inflow, especially in Seyfert galaxies and low-luminosity quasars (P. F. Hopkins et al. 2008). In poststarburst galaxies, supernovae and black hole activity can disperse gas and cause inhomogeneity, albeit briefly (P. F. Hopkins et al. 2008). All these phenomena contribute to the movement of gas toward the galactic center, which can then trigger starbursts as well as feed AGN accretion, which has been verified through numerical simulations (J. C. Mihos & L. Hernquist 1996; T. Di Matteo et al. 2005).

AGNs have also been proposed to provide positive feedback by enhancing star formation in galaxies. Models and simulations have demonstrated that outflows from AGNs can overcompress cold gases to form stars, especially for galaxies in their gas-rich phase (K. Zubovas et al. 2013), for which its effect is dependent on the central AGN's properties (W. E. Clavijo-Bohórquez et al. 2024). Observational evidence supporting this scenario includes the detection of polycyclic aromatic hydrocarbons across various spatial scales in AGN-dominated galaxies (e.g., D. A. Sales et al. 2013; N. L. Zakamska et al. 2015; I. García-Bernete et al. 2021). Quantitatively, black hole accretion rates have been found to correlate with star formation rates when traced using forbidden molecular lines, especially in a galaxy's inner regions (A. M. Diamond-Stanic & G. H. Rieke 2012; D. Esparza-Arredondo et al. 2018; M. Martìnez-Paredes et al. 2019). Although the effect is more pronounced at higher redshifts ($z > 3$; E. Pouliasis et al. 2022), AGN activity does not universally suppress star formation in nearby galaxies (C. R. Mulcahey et al. 2022).

7. GHZ Implications

In reconciling the presence of H_2CO near the hostile Galactic center despite its significance as a biogenic molecule, this paper draws several inferences. H_2CO's high rotational constants (D. Defrees & A. McLean 1986), strong dipole moment (D. R. Johnson et al. 1972), and temperature-dependence of the hyperfine coupling constants (Y. Ellinger et al. 1980) make it resist degradation and furthermore persist, notably in dense MCs that provide shielding effects. H_2CO's biogenic role is also more pivotal in the infancy of COMs, serving as a stepping stone rather than a direct contributor to the emergence or sustenance of life, and many of the broader chemical pathways that occur in MCs may be decoupled from the specific conditions required to sustain life. E. D. Araya et al. (2014), G. Molpeceres et al. (2021), and E. Herbst & R. T. Garrod (2022), in the course of exploring the catalytic processes driving the emergence of COMs in MCs, extemporaneously indicate the intermediary but fleeting nature of H_2CO. Gas-phase and grain-surface processes involving H_2CO in the preliminaries go on to synthesize larger molecules (N. Watanabe & A. Kouchi 2002; K.-J. Chuang et al. 2015; J. B. Bergner et al. 2017; J. T. Carder et al. 2021), including through a three-body mechanism refined by M. Jin & R. T. Garrod (2020) based on G. Fedoseev et al. (2015, 2017) with P. Theulé et al. (2013) in which H_2CO acts a

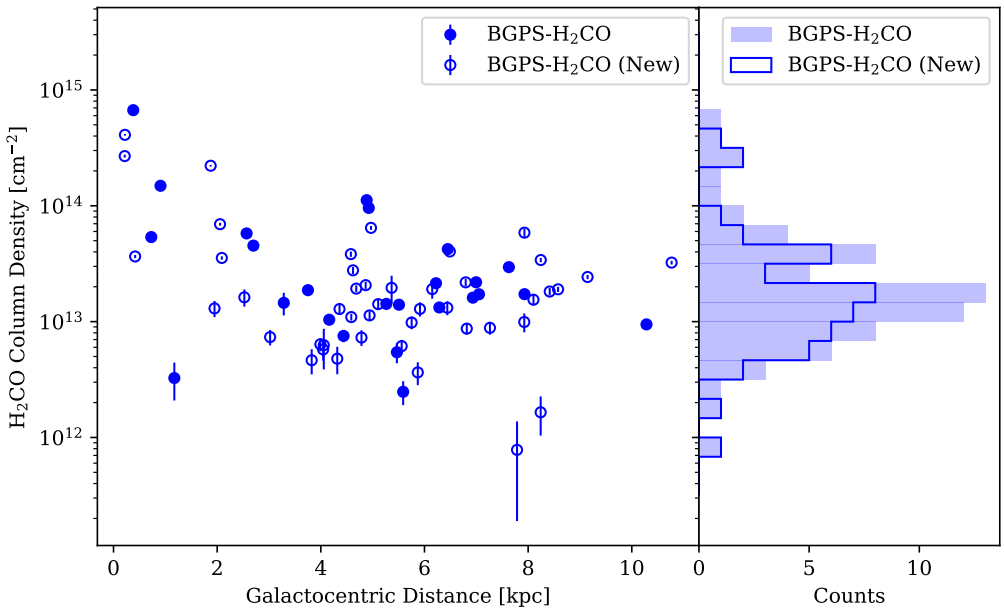

Figure 11. Relation between BGPS-H_2CO galactocentric distances and their column densities. Left panel: Plot of BGPS-H_2CO sources' column densities against galactocentric distances. The Pearson's correlation coefficient for this relation is −0.4622. Right panel: Distribution of the calculated column densities of the BGPS-H_2CO cataloged for sources with cross-match counterparts in MD17.

reactive intermediate, either reacting with hydrogen atoms to form the hydroxymethyl radical (CH_2OH), which further reacts to produce methanol

$$H_2CO + H \rightarrow CH_2OH \quad (3)$$

$$CH_2OH + H \rightarrow CH_3OH \quad (4)$$

or reacting with the formyl radical (HCO) to form glycoaldehyde, a simple sugar precursor which will then undergo further hydrogenation to form ethylene glycol

$$H_2CO + HCO \rightarrow CH_2OHCHO \quad (5)$$

$$CH_2OHCHO + H \rightarrow CH_2OHCH_2OH \quad (6)$$

all of which present enhanced efficiency through the nondiffusive three-body processes, occurring at the more challenging proximities of the Galactic center, rather than its outwards arms. L. Evans et al. (2025) have also discussed the coupling of H_2CO and CH_3OH in protoplanetary disks, further lending credence in expositing H_2CO near the Galactic center might originate from interstellar ice that has been shielded within dense MCs, allowing it to persist despite the hostile conditions.

While H_2CO has been established as an essential biogenic molecule, its widespread distribution in regions across a wide range of galactocentric distances (mainly S. K. Blair et al. 2008, also see references in Section 3) complicates its role as a reliable sole tracer of habitability. Our results show a significant amount of H_2CO detections in the inner Galaxy as in the outer Galaxy priorly documented, as near as 0.2 kpc from the Galactic Center. The location of the cross-matched BGPS-H_2CO sources in the Milky Way are shown in Figure 12. However, the higher levels of ionizing radiation that can photolyse complex molecules (M. Morris & E. Serabyn 1996), higher frequency of supernovae (J. Bland-Hawthorn & M. Cohen 2003), and higher flux of cosmic rays (A. W. Strong et al. 2007) in the environment around the Galactic Center have devastating effects on potential life forms. Increased stellar collisional rates (S. C. Rose et al. 2023) and gravity-induced disruptions (R. Genzel et al. 2010) would also make for an unstable environment for the continuous development of any lifeform that might rise.

As such, with all considerations taken into account, the sole usage of H_2CO as a chemical tracer for GHZ should be tentatively approached. F. Fontani et al. (2022) demonstrated the ubiquitous distribution of organic molecules across diverse galactic environments and argued how this underscores the need for a more rigorous examination of chemical abundance implying habitability. It would benefit significantly from ancillary observations of other key biomolecules, such as ammonia (NH_3), that can react with H_2CO and hydrogen cyanide (HCN) to play a critical role in prebiotic chemistry. For instance, NH_3 can react with H_2CO to produce formamide ($HCONH_2$), a precursor to nucleobases and genetic species (R. Saladino et al. 2012), while HCN is a fundamental building block for the synthesis of amino acids (via Strecker synthesis; A. Strecker 1850; N. Kitadai & S. Maruyama 2018) and nucleotides (via polymerization; J. Oró 1961). Additionally, the codetection of H_2CO and HCN in stable environments, such as protoplanetary disks (K. I. Öberg et al. 2010), could indicate regions conducive to prebiotic chemistry, including the formation of sugars via the formose reaction (A. L. Weber 2005).

Beyond these molecules, the overall presence of NCHOPS elements[8] are also prebiotically significant. These elements are the building blocks of complex biomolecules, including proteins, RNA/DNA, and lipids, which are necessary for the emergence of life (G. Wald 1964; J. A. Baross 2005; M. A. Freire 2022). Phosphorus is a critical component of nucleotides and phospholipids (M. Pasek & D. Lauretta 2007;

[8] Nitrogen, Carbon, Hydrogen, Oxygen, Phosphorus, and Sulfur; the six key elements in prebiotic chemistry of the Universe, with earliest mentions by M. A. Pasek & D. S. Lauretta (2005), N. Prantzos (2007), and M. A. Pasek (2008).

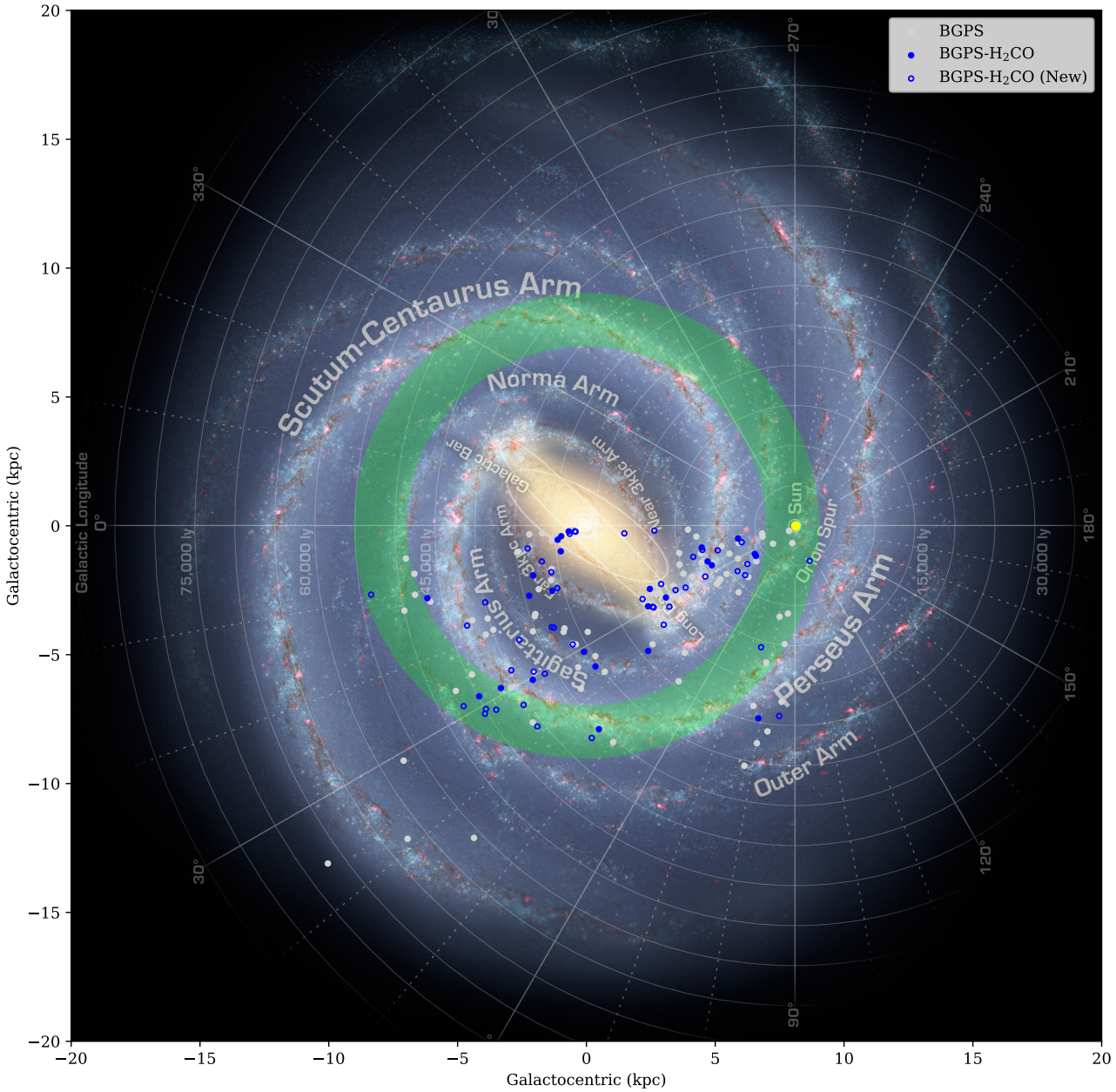

Figure 12. Location of BGPS-H_2CO sources in the Milky Way based on cross-matching with MD17. The yellow spot denotes the location of the Sun, while the green annuli shows the traditional GHZ between 7 and 9 kpc from the Galactic Center. Credit (Milky Way Background): NASA/JPL-Caltech/R. Hurt (SSC/Caltech).

M. A. Pasek et al. 2008), and the discovery of phosphorus bearing molecules such as phosphorus monoxide (PO) and phosphorus mononitride (PN) in the outer Galaxy (WB86-621 at 22.6 kpc from the Galactic Center; L. A. Koelemay et al. 2023) challenges the notion of the barrenness of said region for the formation of life. Another essential element for formation of amino acids e.g., cysteine and methionine (Y. Vallée & S. Youssef-Saliba 2021), is sulfur, which was also observed in a couple star-forming regions (Y. C. Minh 2016), and the absence of sulfur dioxide (SO_2) can be utilized to distinguish exoplanets with hospitable planetary atmospheres and presence of water, further constraining the possibility of life (S. Jordan et al. 2025).[9] Thus, observations of other chemical tracers, particularly NH_3 and HCN, and generally NCHOPS molecules, can further constrain the chemical GHZ in context of the formation of biological prerequisites to the formation of organisms. However, their interpretation must be coupled with the physical constraints (e.g., supernovae frequency, cosmic rays, and stellar density; C. H. Lineweaver et al. 2004; M. Gowanlock et al. 2011), which can disrupt the stability of prebiotic environments and ultimately affect habitability.

Alternatively, the significance of a biogenic precursor being abundantly proximate to the Galactic Center can be expounded further by leveraging the concept of Galactic habitable orbit proposed by J. Baba et al. (2024). The authors offered the theory of a traveling Sun where the dynamic influence of the Galactic bar and spiral arms had the Sun migrating a radial distance of 3.2–4 kpc from its birth radius near the Galactic Center to its present location. This was previously modeled by J. A. Sellwood & J. J. Binney (2002), who showed how stars

[9] The absence signifies that sulfur is actually contained within the atmosphere in an evaporation-deposition cycle, allowing for its participation in biological reactions.

can migrate radially in the Galactic disk through regions with different physical and chemical conditions.

In such manner, to put in the context of this research, a future life-seeding star could traverse different regions of the Galaxy, potentially acquire/store prebiotic molecules and settle in a less-perturbed areas for the essential reactions for an early Earth to occur and not necessarily flourish in the Galactic Center itself. This acquisition, however, rarely occurs directly. Several plausible ways could be during the brief protoplanetary disk phase (C. Qi et al. 2013a, 2013b; J. D. Ilee et al. 2021) or while transiting the dense cores of giant MCs (e.g., S. L. Widicus Weaver & D. N. Friedel 2012). Another possible pathway involves the indirect delivery of biogenic molecules via intermediary bodies such as comets which can preserve material in their ice reservoirs (N. Biver & D. Bockelée-Morvan 2019). S. N. Milam et al. (2006) observed H_2CO in comets C/1995 O1 (Hale-Bopp), C/2002 T7 (LINEAR), and C/2001 Q4 (NEAT) and postulated that organics such as H_2CO may detach from the main cometary bodies and seeded planets or enriched environments that contain planetary systems encountered during their flight, one such mechanism being through photodissociation (P. D. Feldman 2015).

The fact that H_2CO was previously detected at distances as far as 23 kpc should not imply habitability as well because it could be the relic of past dynamical processes, such as galactic mergers, supernova-driven outflows, or the aforementioned stellar migrations, which might have redistributed prebiotic molecules across the galaxy. I. Minchev & B. Famaey (2010) demonstrated that stars migrate radially through resonant scattering and would naturally transport with them the chemical composition they inherited at their birth location, including molecules such as H_2CO. R. A. Ibata et al. (1994, 1995) explicitly discussed the undergoing merger between the Milky Way and the Sagittarius dwarf galaxy causing strong tidal disruptions due to its proximity to the Galactic Center and its radial velocity that would imply the transfer of its constituent matter, including gas molecules. Using the galactic fountain events first delineated by P. R. Shapiro & G. B. Field (1976), J. N. Bregman (1980) in the Milky Way, star formation and supernova activity in a galaxy's disk drive cycles of gas ejection and reaccretion. This is also seen by A. Li et al. (2023) in NGC 2403, where the galactic fountains eject and contribute back to the disk-halo interface, which can then potentially drive the inside-out disk growth and redistribute its composition. The presence of galactic substructures such as the Radcliffe wave, i.e., a massive undulating structure of gas and dust in the Milky Way (J. Alves et al. 2020) which was seen to be oscillating and propagating radially outwards from the Galactic Center (R. Konietzka et al. 2024), also supports the idea of migrating stars gathering prebiotic molecules before settling and prospering with life.

8. Conclusion

In this paper, we report the comprehensive observation of H_2CO absorption and $H_{110\alpha}$ emission in MCs of the Galactic Plane sampled from the BPGS catalog. Using the Nanshan 25 m radio telescope, we identified 88 out of 215 sources exhibiting H_2CO absorption (40.93%), with 59 of them being new detections. Only 11 sources (5.12%) were detected with $H_{110\alpha}$ emission, and based on the H_2CO physical parameters, we confirm that the majority of the BGPS-H_2CO objects are MCs in the early stages of star formation. We also noted the double correlative nature of the H_2CO fluxes with infrared flux, which is thought to be a result of sub-CMB cooling.

In the context of the GHZ, cross-matched BGPS-H_2CO objects show that the H_2CO absorption features are present across a wide range of galactocentric distances, primarily within the inner Galaxy (between 0.216 and 10.769 kpc), which is an underexplored region in terms of the presence of biogenic precursors. Detections of H_2CO in near proximity to the Galactic Center suggest sufficient shielding within dense MCs to preserve COMs, and this challenges the traditional GHZ models that primarily rely on metallicity and catastrophic events as limiting factors. Our findings highlight the need to incorporate biogenic precursors (e.g., H_2CO) as a defining criterion of GHZ in the Milky Way. The negative-correlation observed between H_2CO's detection fraction and column density with galactocentric distances also enhances the role of dynamic processes in redistributing prebiotically plausible molecules in the Galaxy.

While H_2CO alone may present some bias as a habitability tracer, its presence in conjunction with auxiliary key prebiotic molecules, such as NH_3, HCN, and other NCHOPS molecules in general, may provide better outcomes as a GHZ indicator. Future studies should also incorporate physical limiters for habitability (e.g., AGN influence, supernova frequency, metallicity, and stellar density) to further constrain the inner and outer radii of the GHZ. By expanding the chemical framework for defining the GHZ, our findings contribute to the broader effort of understanding the origins of life in the Universe and refine the search for prebiotic chemistry beyond our Earth.

Acknowledgments

We sincerely thank the staff of the Nanshan Observatory for their invaluable support during the observations. The observations for this study were conducted using the Nanshan 25 m Radio Telescope, which is operated by the Key Laboratory of Radio Astronomy, Chinese Academy of Sciences. The Nanshan 25 m Radio Telescope is partly supported by the Operation, Maintenance, and Upgrading Fund for Astronomical Telescopes and Facility Instruments, budgeted from the Ministry of Finance of China (MOF) and administered by the Chinese Academy of Sciences (CAS). This work was partly funded by the National Key R&D Program of China under grant Nos. 2022YFA1603103 and 2023YFA1608002. We warmly thank Dr. Nami Sakai (Chief Scientist, Star and Planet Formation Laboratory, RIKEN) and Dr. Yao-Lun Yang (RIKEN) for their invaluable insights during the formative stages of this work and a special thanks to Dr. Ross A. Burns (RIKEN Cluster for Pioneering Research) for his feedback and encouragement. We also extend our gratitude to the anonymous referee for the insightful comments and suggestions, which significantly improved the quality of this manuscript.

Facility: CVN (Nanshan 25-m).

Software: GILDAS (Gildas Team 2013), numpy (C. R. Harris et al. 2020), astropy (The Astropy Collaboration et al. 2022), matplotlib (J. D. Hunter 2007).

Appendix A
Selected BGPS Source Parameters

Table 2 shows the list of all the selected BGPS sources with their H_2CO and H_{110a} detection flags.

Table 2
List of the BGPS Sources Observed Using Nanshan 25 m

Source	R.A. (J2000)	Decl. (J2000)	l	b	$S_{\rm BGPS}$	H_2CO	$H_{110\alpha}$
	(hh:mm:ss)	(dd:mm:ss.ss)	(deg)	(deg)	(Jy)	(Detected?)	(Detected?)
(1)	(2)	(3)	(4)	(5)	(6)	(7)	(8)
BGPS0352	17:46:50	−27:53:26.27	1.032	0.316	2.745	N	N
BGPS0512	17:48:56	−27:44:37.00	1.398	−0.006	2.282	Y	N
BGPS0523	17:47:48	−27:33:25.14	1.428	0.306	2.963	Y	N
BGPS0548	17:49:57	−27:44:14.28	1.518	−0.194	2.941	Y	N
BGPS0598	17:50:55	−27:40:25.07	1.684	−0.348	1.170	N	N
⋮							

Note. Columns: (1) BGPS source name; (2) and (3) Coordinates in equatorial coordinate system; (4) and (5) Coordinates in Galactic coordinate system; (6) BGPS 1.1 mm continuum flux; (7) and (8) H_2CO and $H_{110\alpha}$ detection flags i.e., "Y" denotes detection and "N" denotes nondetection.

(This table is available in its entirety in machine-readable form in the online article.)

Appendix B
Observational Parameters of BGPS Sources with H_2CO Detection

Table 3 lists the observational parameters of the BGPS sources with H_2CO detections.

Table 3
Observational Parameters of the BGPS Sources with H_2CO Detection

Source	Date	Elevation	$T_{\rm sys}$	σ	$n(H_2CO)$	$n(H_{110\alpha})$
		(°)	(K)	(K)		
(1)	(2)	(3)	(4)	(5)	(6)	(7)
BGPS0512	2013-08-14 16:05:15.000	15.3188	34.4313	0.0229	4	0
BGPS0523	2013-08-14 16:32:15.000	13.2965	35.6863	0.0234	2	0
BGPS0548	2013-08-14 16:59:15.000	10.8040	39.2719	0.0182	4	0
BGPS0647	2014-02-17 01:58:15.000	18.9745	22.1199	0.0128	3	0
BGPS0657	2014-02-17 02:24:55.000	19.1751	22.1199	0.0302	8	0
⋮						

Note. Columns: (1) BGPS source name; (2) Observation date and time; (3) Observation elevation; (4) Antenna system temperature; (5) rms noise; (6, 7) Number of H_2CO and $H_{110\alpha}$ lines detected.

(This table is available in its entirety in machine-readable form in the online article.)

Appendix C
Gaussian Fitting Results of all H_2CO and $H_{110\alpha}$ Lines

Tables 4 and 5 provide the Gaussian fitting results of all H_2CO and H_{110a} lines detected respectively.

Table 4
Gaussian Fitting Parameters of all H_2CO Lines Detected

Source	Brightness Temp.	Velocity	FWHM	Integrated Int.	Baseline rms	Line rms
	(K)	(km s^{-1})	(km s^{-1})	(K km s^{-1})	(K)	(K)
(1)	(2)	(3)	(4)	(5)	(6)	(7)
BGPS0512 MC1	−0.0578	−53.9 ± 0.4	4.0 ± 1.0	−0.25 ± 0.05	0.0229	0.0197
BGPS0512 MC2	−0.1930	−27.53 ± 0.31	17.1 ± 0.7	−3.50 ± 0.24	0.0229	0.0197
BGPS0512 MC3	−0.0833	−2.4 ± 1.6	38.4 ± 2.7	−3.41 ± 0.27	0.0229	0.0197
BGPS0512 MC4	−0.3350	79.41 ± 0.22	42.4 ± 0.6	−15.15 ± 0.16	0.0229	0.0197
BGPS0523 MC1	−0.0365	−2.8 ± 1.6	26.1 ± 3.2	−1.01 ± 0.12	0.0234	0.0181
⋮						

Note. Columns: (1) BGPS source name with MC number; (2) Brightness temperature of the line; (3) Central velocity of the line; (4) FWHM of the line; (5) Integrated intensity of the line; (6) and (7) Baseline and line rms noise.

(This table is available in its entirety in machine-readable form in the online article.)

Table 5
Gaussian Fitting Parameters of all $H_{110\alpha}$ Lines Detected

Source	Brightness Temp. (K)	Velocity (km s^{-1})	FWHM (km s^{-1})	Integrated Int. (K km s^{-1})	Baseline rms (K)	Line rms (K)
(1)	(2)	(3)	(4)	(5)	(6)	(7)
BGPS1326 HIIa	0.0222	72.0 ± 1.4	18.1 ± 3.0	0.43 ± 0.06	0.0150	0.0121
BGPS1520 HIIa	0.0547	31.8 ± 0.8	22.2 ± 1.9	1.29 ± 0.09	0.0192	0.0176
BGPS2045 HIIa	0.0438	37.8 ± 1.0	29.1 ± 2.4	1.36 ± 0.09	0.0162	0.0167
BGPS2094 HIIa	0.0911	35.8 ± 0.7	28.3 ± 1.6	2.74 ± 0.13	0.0232	0.0210
BGPS2313 HIIa	0.0171	38.4 ± 1.3	19.4 ± 2.4	0.35 ± 0.04	0.0101	0.0092
BGPS4244 HIIa	0.0341	106.0 ± 0.7	22.2 ± 1.5	0.80 ± 0.05	0.0100	0.0134
BGPS4372 HIIa	0.0328	109.9 ± 0.9	32.0 ± 1.9	1.12 ± 0.06	0.0101	0.0093
BGPS5385 HIIa	0.0199	79.9 ± 1.1	16.9 ± 2.9	0.36 ± 0.05	0.0111	0.0106
BGPS5884 HIIa	0.0268	59.3 ± 1.0	25.7 ± 2.6	0.73 ± 0.06	0.0101	0.0106
BGPS5910 HIIa	0.0242	65.8 ± 1.2	23.3 ± 2.9	0.60 ± 0.06	0.0104	0.0089
BGPS5910 HIIb	0.0127	88.2 ± 1.6	10.7 ± 2.5	0.14 ± 0.04	0.0104	0.0089
BGPS6661 HIIa	0.0176	−46.8 ± 1.4	24.8 ± 2.7	0.46 ± 0.05	0.0099	0.0089
BGPS6661 HIIb	0.0238	27.8 ± 1.2	27.3 ± 2.5	0.69 ± 0.05	0.0099	0.0089

Note. Columns: (1) BGPS source name with H II identifier; (2) Brightness temperature of the line; (3) Central velocity of the line; (4) FWHM of the line; (5) Integrated intensity of the line; (6) and (7) Baseline and line rms noise.

(This table is available in its entirety in machine-readable form in the online article.)

Appendix D
Master BGPS-H_2CO Catalog

Table 6 shows the listings contained in the master BGPS-H_2CO catalog.

Table 6
Entries of the Master BGPS-H_2CO Catalog

Entry	Units	Description
BGPS	...	BGPS source name
RAdeg	deg	R.A. (J2000)
DEdeg	deg	decl. (J2000)
l	deg	Galactic longitude
b	deg	Galactic latitude
S_{BGPS}	Jy	BGPS 1.1 mm continuum flux
H_2CO	...	H_2CO detection flag ("Y": detection, "N": nondetection)
$H_{110\alpha}$	...	$H_{110\alpha}$ detection flag ("Y": detection, "N": nondetection)
First detection	...	First detection flag ("Y": first detection, "N": previously detected)
$N(H_2CO)$	...	Number of H_2CO absorption lines detected
$N(H_{110\alpha})$	...	Number of $H_{110\alpha}$ emission lines detected
T_{sys}	K	Antenna system temperature
$T(H_2CO)$	K	Brightness temperature of H_2CO line
$S(H_2CO)$	Jy	Flux density of H_2CO line
$V(H_2CO)$	km s^{-1}	Central velocity of H_2CO line
FWHM(H_2CO)	km s^{-1}	FWHM of H_2CO line
$T_{int}(H_2CO)$	K km s^{-1}	Integrated intensity of H_2CO line
$T(H_{110\alpha})$	K	Brightness temperature of $H_{110\alpha}$ line
$S(H_{110\alpha})$	Jy	Flux density of $H_{110\alpha}$ line
$V(H_{110\alpha})$	km s^{-1}	Central velocity of $H_{110\alpha}$ line
FWHM($H_{110\alpha}$)	km s^{-1}	FWHM of $H_{110\alpha}$ line
$T_{int}(H_{110\alpha})$	K km s^-1	Integrated intensity of $H_{110\alpha}$ line
R_{gal}	kpc	Galactocentric distance based on cross-matching with MD17
KD	kpc	Kinematic distance based on cross-matching with MD17
z_{gal}	kpc	Distance to Galactic midplane based on cross-matching with MD17
V(^{12}CO)	km s^{-1}	Central velocity of ^{12}CO line based on cross-matching with MD17
τ_{app}	...	Derived apparent optical depth based on H_2CO line
$N(H_2CO)$	cm^{-2}	Derived H_2CO column density based on H_2CO line

Note. The full master table includes all the selected BGPS sources and other information including H_2CO parameters, $H_{110\alpha}$ parameters, MD17 cross-matched parameters, and derived H_2CO parameters. If the data is unavailable, the columns will be masked appropriately. Spectral line results and derived parameters are accompanied with their standard deviations.

(This table is available in its entirety in machine-readable form in the online article.)

ORCID iDs

N. B. Baharin https://orcid.org/0009-0009-4694-5097

References

Adande, G. R., Woolf, N. J., & Ziurys, L. M. 2013, AsBio, 13, 439
Aguirre, J. E., Ginsburg, A. G., Dunham, M. K., et al. 2010, ApJS, 192, 4
Alves, J., Zucker, C., Goodman, A. A., et al. 2020, Natur, 578, 237
Anderson, L. D., Bania, T. M., Balser, D. S., & Rood, R. T. 2012, ApJ, 754, 62
Araya, E. D., Dieter-Conklin, N., Goss, W. M., & Andreev, N. 2014, ApJ, 784, 129
Araya, E. D., Hofner, P., Goss, W. M., et al. 2008, ApJS, 178, 330
Araya, E. D., Olmi, L., Ortiz, J. M., et al. 2015, ApJS, 221, 10
Baba, J., Tsujimoto, T., & Saitoh, T. R. 2024, ApJL, 976, L29
Balbi, A., Hami, M., & Kovačević, A. 2020, Life, 10, 132
Bally, J., & Scoville, N. Z. 1980, ApJ, 239, 121
Baross, J. A. 2005, The Environmental Roots of the Origin of Life (Tucson, AZ: Univ. Arizona Press), 1
Bergner, J. B., Öberg, K. I., & Rajappan, M. 2017, ApJ, 845, 29
Bernal, J. J., Sephus, C. D., & Ziurys, L. M. 2021, ApJ, 922, 106
Biver, N., & Bockelée-Morvan, D. 2019, ESC, 3, 1550
Blair, S. K., Magnani, L., Brand, J., & Wouterloot, J. G. 2008, AsBio, 8, 59
Bland-Hawthorn, J., & Cohen, M. 2003, ApJ, 582, 246

Boamah, M. D., Sullivan, K. K., Shulenberger, K. E., et al. 2014, FaDi, 168, 249
Bregman, J. N. 1980, ApJ, 236, 577
Brunt, C. M., Kerton, C. R., & Pomerleau, C. 2003, ApJS, 144, 47
Bu, J., Esimbek, J., Zhou, J., et al. 2024, RAA, 24, 075022
Carder, J. T., Ochs, W., & Herbst, E. 2021, MNRAS, 508, 1526
Caselli, P., & Ceccarelli, C. 2012, A&ARv, 20, 56
Chen, X., Shen, Z.-Q., Li, X.-Q., et al. 2017, MNRAS, 466, 4364
Chuang, K.-J., Fedoseev, G., Ioppolo, S., van Dishoeck, E., & Linnartz, H. 2015, MNRAS, 455, 1702
Clavijo-Bohórquez, W. E., de Gouveia Dal Pino, E. M., & Melioli, C. 2024, MNRAS, 535, 1696
Costanzo, G., Saladino, R., Crestini, C., Ciciriello, F., & Di Mauro, E. 2007, BMCEB, 7, S1
Coutens, A., Persson, M. V., Jørgensen, J. K., Wampfler, S. F., & Lykke, J. M. 2015, A&A, 576, A5
Cuadrado, S., Goicoechea, J. R., Cernicharo, J., et al. 2017, A&A, 603, A124
Dame, T. M., Hartmann, D., & Thaddeus, P. 2001, ApJ, 547, 792
Darling, J., & Zeiger, B. 2012, ApJL, 749, L33
Defrees, D., & McLean, A. 1986, CPL, 131, 403
Di Matteo, T., Springel, V., & Hernquist, L. 2005, Natur, 433, 604
Diamond-Stanic, A. M., & Rieke, G. H. 2012, ApJ, 746, 168
Du, Z. M., Zhou, J. J., Esimbek, J., Han, X. H., & Zhang, C. P. 2011, A&A, 532, A127
Ehrenfreund, P., Irvine, W., Becker, L., et al. 2002, RPPh, 65, 1427
Ellinger, Y., Pauzat, F., Barone, V., Douady, J., & Subra, R. 1980, JChPh, 72, 6390
Esparza-Arredondo, D., González-Martín, O., Dultzin, D., et al. 2018, ApJ, 859, 124
Evans, L., Booth, A. S., Walsh, C., et al. 2025, ApJ, 982, 62
Fedoseev, G., Chuang, K.-J., Ioppolo, S., et al. 2017, ApJ, 842, 52
Fedoseev, G., Cuppen, H. M., Ioppolo, S., Lamberts, T., & Linnartz, H. 2015, MNRAS, 448, 1288
Feldman, P. D. 2015, ApJ, 812, 115
Fontani, F., Colzi, L., Bizzocchi, L., et al. 2022, A&A, 660, A76
Forgan, D., Dayal, P., Cockell, C., & Libeskind, N. 2016, IJAsB, 16, 60
Freire, M. A. 2022, BiSys, 211, 104547
García-Bernete, I., Rigopoulou, D., Alonso-Herrero, A., et al. 2021, MNRAS, 509, 4256
Genzel, R., Eisenhauer, F., & Gillessen, S. 2010, RvMP, 82, 3121
Gerin, M., Liszt, H., Pety, J., & Faure, A. 2024, A&A, 686, A49
Gildas Team 2013, GILDAS: Grenoble Image and Line Data Analysis Software, Astrophysics Source Code Library, ascl:1305.010
Ginsburg, A., Bally, J., Battersby, C., et al. 2015a, A&A, 573, A106
Ginsburg, A., Walsh, A., Henkel, C., et al. 2015b, A&A, 584, L7
Gong, Y., Ortiz-León, G. N., Rugel, M. R., et al. 2023, A&A, 678, A130
Gonzalez, G. 2005, OLEB, 35, 555
Gonzalez, G., Brownlee, D., & Ward, P. 2001, Icar, 152, 185
Gowanlock, M., Patton, D., & McConnell, S. 2011, AsBio, 11, 855
Guo, W. H., Esimbek, J., Di Tang, X., et al. 2016, Ap&SS, 361, 264
Harris, C. R., Millman, K. J., van der Walt, S. J., et al. 2020, Natur, 585, 357
Herbst, E., & Garrod, R. T. 2022, FrASS, 8, 209
Heyer, M., Krawczyk, C., Duval, J., & Jackson, J. M. 2009, ApJ, 699, 1092
Hollenbach, D. J., & Tielens, A. G. G. M. 1999, RvMP, 71, 173
Hopkins, P. F., Hernquist, L., Cox, T. J., & Kereš, D. 2008, ApJS, 175, 356
Hunter, J. D. 2007, CSE, 9, 90
Ibata, R. A., Gilmore, G., & Irwin, M. J. 1994, Natur, 370, 194
Ibata, R. A., Gilmore, G., & Irwin, M. J. 1995, MNRAS, 277, 781
Ilee, J. D., Walsh, C., Booth, A. S., et al. 2021, ApJS, 257, 9
Jin, M., & Garrod, R. T. 2020, ApJS, 249, 26
Johnson, D. R., Lovas, F. J., & Kirchhoff, W. H. 1972, JPCRD, 1, 1011
Jordan, S., Shorttle, O., & Rimmer, P. B. 2025, SciA, 11, eadp8105
Keto, E. 2002, ApJ, 580, 980
Keto, E., Zhang, Q., & Kurtz, S. 2008, ApJ, 672, 423
Khan, S., Rugel, M. R., Brunthaler, A., et al. 2024, A&A, 689, A81
Kitadai, N., & Maruyama, S. 2018, GeoFr, 9, 1117
Koch, E. W., Rosolowsky, E. W., Schruba, A., et al. 2019, MNRAS, 485, 2324
Koelemay, L. A., Gold, K. R., & Ziurys, L. M. 2023, Natur, 623, 292
Kolpak, M. A., Jackson, J. M., Bania, T. M., Clemens, D. P., & Dickey, J. M. 2003, ApJ, 582, 756
Komesh, T., Esimbek, J., Baan, W., et al. 2019, ApJ, 874, 172
Konietzka, R., Goodman, A. A., Zucker, C., et al. 2024, Natur, 628, 62
Koulouridis, E., Plionis, M., Chavushyan, V., et al. 2006, ApJ, 639, 37
Li, A., Fraternali, F., Marasco, A., et al. 2023, MNRAS, 520, 147
Lineweaver, C. H., Fenner, Y., & Gibson, B. K. 2004, Sci, 303, 59
Liszt, H. S., & Pety, J. 2016, ApJ, 823, 124
Mahmut, U., Esimbek, J., Baan, W., et al. 2024, MNRAS, 528, 577
Mangum, J. G., & Shirley, Y. L. 2015, PASP, 127, 266
Martìnez-Paredes, M., Aretxaga, I., González-Martìn, O., et al. 2019, ApJ, 871, 190
Menten, K. M., & Reid, M. J. 1996, ApJL, 465, L99
Mihos, J. C., & Hernquist, L. 1996, ApJ, 464, 641
Milam, S. N., Remijan, A. J., Womack, M., et al. 2006, ApJ, 649, 1169
Minchev, I., & Famaey, B. 2010, ApJ, 722, 112
Minh, Y. C. 2016, JPhCS, 728, 052007
Miville-Deschênes, M.-A., Murray, N., & Lee, E. J. 2017, ApJ, 834, 57
Molpeceres, G., Kästner, J., Fedoseev, G., et al. 2021, JPCL, 12, 10854
Morris, M., & Serabyn, E. 1996, ARA&A, 34, 645
Mulcahey, C. R., Leslie, S. K., Jackson, T. M., et al. 2022, A&A, 665, A144
Nari, N., Dumusque, X., Hara, N. C., et al. 2025, A&A, 693, A297
Öberg, K. I., Qi, C., Fogel, J. K. J., et al. 2010, ApJ, 720, 480
Oró, J. 1961, Natur, 191, 1193
Pabst, C. H. M., Goicoechea, J. R., Cuadrado, S., et al. 2024, A&A, 688, A7
Pasek, M., & Lauretta, D. 2007, OLEB, 38, 5
Pasek, M. A. 2008, PNAS, 105, 853
Pasek, M. A., Kee, T. P., Bryant, D. E., Pavlov, A. A., & Lunine, J. I. 2008, AngCh International Edition, 47, 7918
Pasek, M. A., & Lauretta, D. S. 2005, AsBio, 5, 515
Pouliasis, E., Mountrichas, G., Georgantopoulos, I., et al. 2022, A&A, 667, A56
Prantzos, N. 2007, SSRv, 135, 313
Punanova, A. F., Borshcheva, K., Fedoseev, G. S., et al. 2025, MNRAS, 537, 3686
Qi, C., Öberg, K. I., & Wilner, D. J. 2013a, ApJ, 765, 34
Qi, C., Öberg, K. I., Wilner, D. J., & Rosenfeld, K. A. 2013b, ApJL, 765, L14
Quireza, C., Rood, R. T., Balser, D. S., & Bania, T. M. 2006, ApJS, 165, 338
Reid, M., & Honma, M. 2014, ARA&A, 52, 339
Reid, M. J., Menten, K. M., Brunthaler, A., et al. 2019, ApJ, 885, 131
Roman-Duval, J., Jackson, J. M., Heyer, M., et al. 2009, ApJ, 699, 1153
Rose, S. C., Naoz, S., Sari, R., & Linial, I. 2023, ApJ, 955, 30
Rosolowsky, E., Dunham, M. K., Ginsburg, A., et al. 2010, ApJS, 188, 123
Ruffle, P. M. E., Millar, T. J., Roberts, H., et al. 2007, ApJ, 671, 1766
Sagear, S., & Ballard, S. 2023, PNAS, 120, e2217398120
Saladino, R., Crestini, C., Pino, S., Costanzo, G., & Di Mauro, E. 2012, PhLRv, 9, 84
Sales, D. A., Pastoriza, M. G., Riffel, R., & Winge, C. 2013, MNRAS, 429, 2634
Sandqvist, A., & Bernes, C. 1980, in IAU Symp. 87, Interstellar Molecules, ed. B. H. Andrew (Cambridge: Cambridge Univ. Press), 103
Sellwood, J. A., & Binney, J. J. 2002, MNRAS, 336, 785
Sewilo, M., Churchwell, E., Kurtz, S., Goss, W. M., & Hofner, P. 2004, ApJ, 605, 285
Shapiro, P. R., & Field, G. B. 1976, ApJ, 205, 762
Snell, R. L., Carpenter, J. M., & Heyer, M. H. 2002, ApJ, 578, 229
Snyder, L. E., Buhl, D., Zuckerman, B., & Palmer, P. 1969, PhRvL, 22, 679
Spitoni, E., Matteucci, F., & Sozzetti, A. 2014, MNRAS, 440, 2588
Strecker, A. 1850, Justus Liebigs Annalen der Chemie, 75, 27
Strong, A. W., Moskalenko, I. V., & Ptuskin, V. S. 2007, ARNPS, 57, 285
Tang, X.-D., Esimbek, J., Zhou, J.-J., Wu, G., & Okoh, D. 2014, RAA, 14, 959
The Astropy Collaboration, Price-Whelan, A. M., Lim, P. L., et al. 2022, ApJ, 935, 167
Theulé, P., Duvernay, F., Danger, G., et al. 2013, AdSpR, 52, 1567
Townes, C. H., & Cheung, A. C. 1969, ApJL, 157, L103
Troscompt, N., Faure, A., Maret, S., et al. 2009, A&A, 506, 1243
Tucker, W. H. 1981, in NASA Conf. Proc, Life in the universe, Vol. 2156 ed. J. Billingham (Cambridge, MA: MIT Press), 287
Turner, B. E. 1993, ApJ, 410, 140
Vallée, Y., & Youssef-Saliba, S. 2021, Synthesis, 53, 2798
Vukotić, B., Steinhauser, D., Martinez-Aviles, G., et al. 2016, MNRAS, 459, 3512
Wald, G. 1964, PNAS, 52, 595
Watanabe, N., & Kouchi, A. 2002, ApJL, 571, L173
Weber, A. L. 2005, OLEB, 35, 523
Wenger, T. V., Balser, D. S., Anderson, L. D., & Bania, T. M. 2018, ApJ, 856, 52
Widicus Weaver, S. L., & Friedel, D. N. 2012, ApJS, 201, 16
Yan, Y. T., Zhang, J. S., Henkel, C., et al. 2019, ApJ, 877, 154
Yuan, Y., Esimbek, J., Zhou, J. J., et al. 2014, Ap&SS, 352, 521
Zahorecz, S., Jimenez-Serra, I., Testi, L., et al. 2021, A&A, 653, A45
Zakamska, N. L., Lampayan, K., Petric, A., et al. 2015, MNRAS, 455, 4191
Zeng, S., Jiménez-Serra, I., Rivilla, V. M., et al. 2018, MNRAS, 478, 2962
Zhao, X., Tang, X. D., Henkel, C., et al. 2024, A&A, 687, A207
Zhu, C., Turner, A. M., Meinert, C., & Kaiser, R. I. 2020, ApJ, 889, 134
Ziurys, L. M. 2018, in Interstellar Molecules and their Prebiotic Potential, ed. V. M. Kolb (Boca Raton, FL: CRC Press), 147
Zubovas, K., Nayakshin, S., King, A., & Wilkinson, M. 2013, MNRAS, 433, 3079